

Microstructural evolution and strengthening mechanism of aligned steel fiber cement-based tail backfills exposed to electromagnetic induction

Xihao Li, Shuai Cao, and Erol Yilmaz

Cite this article as:

Xihao Li, Shuai Cao, and Erol Yilmaz, Microstructural evolution and strengthening mechanism of aligned steel fiber cement-based tail backfills exposed to electromagnetic induction, *Int. J. Miner. Metall. Mater.*, 31(2024), No. 11, pp. 2390-2403. <https://doi.org/10.1007/s12613-024-2985-6>

View the article online at [SpringerLink](#) or [IJMMM Webpage](#).

Articles you may be interested in

Yu-ye Tan, Elmo Davide, Yu-cheng Zhou, Wei-dong Song, and Xiang Meng, [Long-term mechanical behavior and characteristics of cemented tailings backfill through impact loading](#), *Int. J. Miner. Metall. Mater.*, 27(2020), No. 2, pp. 140-151. <https://doi.org/10.1007/s12613-019-1878-6>

Yu-ye Tan, Xin Yu, Davide Elmo, Lin-hui Xu, and Wei-dong Song, [Experimental study on dynamic mechanical property of cemented tailings backfill under SHPB impact loading](#), *Int. J. Miner. Metall. Mater.*, 26(2019), No. 4, pp. 404-416. <https://doi.org/10.1007/s12613-019-1749-1>

Di Wu, Run-kang Zhao, Chao-wu Xie, and Shuai Liu, [Effect of curing humidity on performance of cemented paste backfill](#), *Int. J. Miner. Metall. Mater.*, 27(2020), No. 8, pp. 1046-1053. <https://doi.org/10.1007/s12613-020-1970-y>

Qian Zhou, Juan-hong Liu, Ai-xiang Wu, and Hong-jiang Wang, [Early-age strength property improvement and stability analysis of unclassified tailing paste backfill materials](#), *Int. J. Miner. Metall. Mater.*, 27(2020), No. 9, pp. 1191-1202. <https://doi.org/10.1007/s12613-020-1977-4>

Li Wang, Chao-fang Dong, Cheng Man, Ya-bo Hu, Qiang Yu, and Xiao-gang Li, [Effect of microstructure on corrosion behavior of high strength martensite steel—A literature review](#), *Int. J. Miner. Metall. Mater.*, 28(2021), No. 5, pp. 754-773. <https://doi.org/10.1007/s12613-020-2242-6>

Min Zhu, Qiang Zhang, Yong-feng Yuan, and Shao-yi Guo, [Effect of microstructure and passive film on corrosion resistance of 2507 super duplex stainless steel prepared by different cooling methods in simulated marine environment](#), *Int. J. Miner. Metall. Mater.*, 27(2020), No. 8, pp. 1100-1114. <https://doi.org/10.1007/s12613-020-2094-0>





IJMMM WeChat



QQ author group

Microstructural evolution and strengthening mechanism of aligned steel fiber cement-based tail backfills exposed to electromagnetic induction

Xihao Li^{1,2}, Shuai Cao^{1,2},, and Erol Yilmaz³,

1) School of Civil and Resources Engineering, University of Science and Technology Beijing, Beijing 100083, China

2) State Key Laboratory of High-Efficient Mining and Safety of Metal Mines of Ministry of Education, University of Science and Technology Beijing, Beijing 100083, China

3) Department of Civil Engineering, Geotechnical Division, Recep Tayyip Erdogan University, Fener Rize TR53100, Turkey

(Received: 14 May 2024; revised: 31 July 2024; accepted: 3 August 2024)

Abstract: Cemented tailings backfill (CTB) not only boosts mining safety and cuts surface environmental pollution but also recovers ores previously retained as pillars, thereby improving resource utilization. The use of alternative reinforcing products, such as steel fiber (SF), has continuously strengthened CTB into SFCTB. This approach prevents strength decreases over time and reinforces its long-term durability, especially when mining ore in adjacent underground stopes. In this study, various microstructure and strength tests were performed on SFCTB, considering steel fiber ratio and electromagnetic induction strength effects. Lab findings show that combining steel fibers and their distribution dominantly influences the improvement of the fill's strength. Fill's strength rises by fiber insertion and has an evident correlation with fiber insertion and magnetic induction strength. When magnetic induction strength is 3×10^{-4} T, peak uniaxial compressive stress reaches 5.73 MPa for a fiber ratio of 2.0vol%. The cracks' expansion mainly started from the specimen's upper part, which steadily expanded downward by increasing the load until damage occurred. The doping of steel fiber and its directional distribution delayed crack development. When the doping of steel fiber was 2.0vol%, SFCTBs showed excellent ductility characteristics. The energy required for fills to reach destruction increases when steel-fiber insertion and magnetic induction strength increase. This study provides notional references for steel fibers as underground filling additives to enhance the fill's durability in the course of mining operations.

Keywords: electromagnetic induction; steel fiber; cemented tailings backfill; strength; microstructure

1. Introduction

Mining, which involves extracting valuable minerals from the earth, plays a crucial role in the growth of a country's economy [1]. However, with the gradual depletion of shallow and high-grade ore resources at the surface [2], the deep high-ground pressure and the massive generation of tailings have become two problems that must be addressed during the mining process [3–5]. To effectively treat tailings [6], improve mining safety [7], and reduce surface environmental pollution [8], scholars and practitioners most often investigate applying cement-based tail backfill methods for the effective and safe management of underground mined-out stopes [9–11]. Cement-based tail backfill (CTB: a combination of cement, tailings, and water with a small number of mineral/chemical additives) is broadly used in most mines because of its low-cost, easy-to-implement, and environmentally friendly properties [12–13]. CTB technology also can recover precious and rare metals [14], as well as ores that were previously retained as pillars [15], thereby improving overall resource utilization [16]. However, despite its many advantages, the CTB system still faces some persuasive

problems [17]. For example, the fill's strength and stability must be further improved, as well as its efficiency and economy [18–19].

In recent years, most practitioners and researchers have directed in-depth indoor lab/field testing on strength features and microstructure of cement-based backfills to continuously promote CPB technique development [20–23]. The addition of specific additives, such as fibers, to the fill matrix can evidently enhance its strength properties [24–27]. Considering the leading disadvantages (e.g., brittleness) of cement-based materials, using fibers as dispersed reinforcements within the matrix could be inhibited to form a composite product of high quality for a wide range of applications [28–29]. Among others, steel fibers are regularly preferred in cement-based materials because of their high tensile strength and thermal expansion [30]. The composite can display strain hardening and deformation hardening behavior when appropriately attached to a cement-based matrix, thereby remarkably enhancing the strengths [31–32]. Xue *et al.* [33–34] and Huang *et al.* [35] explored experimentally that mixing polypropylene and glass fibers in CTB specimens not only improves the uniaxial compressive and flexural strengths but

 Corresponding authors: Shuai Cao E-mail: sandy_cao@ustb.edu.cn; Erol Yilmaz E-mail: erol.yilmaz@erdogan.edu.tr

© University of Science and Technology Beijing 2024

also effectively inhibits the expansion of cracks. Wang *et al.* [36] adopted rice straw ash to substitute part of the binder within CTB specimens. They found that the fill's strength disclosed a growing inclination by increasing the substitution rate of rice straw ash in a certain range. Guo *et al.* [37] established that adding recycled tire polymer fibers (RTPF) to CTB implicitly improved its mechanical properties. This finding was predominantly attributed to RTPF's excellent pore size distribution and long-term hydration properties. Researchers [38–40] have found that the fiber's connecting impact fulfills a momentous duty in deterring crack extension and enhancing the matrix's toughness and mechanical properties.

However, the fibers' chaotic scattering within the fill limits their bridging efficiency [41]. Crack bridging efficiency becomes high if fibers are well oriented and distributed analogous to the main tensile stress direction [42–43]. If fibers are randomly distributed within the matrix, then their capacity to tie fissures/cracks will not be fully utilized [44–46]. To solve this problem, Huang *et al.* [47] adopted an L-designed tool, which significantly improved ultra-high performance concrete (UHPC) steel fibers' orientation and substantially enhanced their mechanical properties. Javahershenas *et al.* [48] evaluated the brittleness index of steel fiber reinforced concrete (SFRC) as a result of diverse exposure intervals by modulating SFRC's exposure time to a standardized magnetic area. They verified that SFRC's strength exhibited an increasing trend with time. Yoo *et al.* [49] released that the fiber number at cracks increased with increasing fiber ratio within the fill matrix, incrementing the bonding space between fiber and matrix, as well as the fiber's linking impact. Qing *et al.* [50] found that the fiber-reinforced concrete's flexural/tensile/shear/fracture characteristics were significantly higher than those of non-fiber-reinforced concrete, having randomly distributed fibers and excellent resistance at

diverse strain rates. Li *et al.* [51] elucidated experimentally that positioning fibers within a cementitious composite matrix influences water movement and seriously affects the fill's microstructure/bonding properties around the steel fibers. Mu *et al.* [52–53] analyzed the modeling/experimental results and concluded that the reinforcing impact of steel fiber's aligned distribution is significantly better than the random distribution's enhancement effect.

At present, studies on cement-based composites armored by steel fiber focus on the impact of performance on high-performance cementitious products, such as concrete. However, studies considering the direction of fiber distribution to further augment the fill's strength features are limited. Hence, in the current investigation, the combined effects of varying steel fiber ratios and magnetic induction intensities on the stress–strain curve, strength, and microstructure of backfill were systematically examined using uniaxial testing and scanning electron microscopy (SEM) microanalysis.

2. Experimental

2.1. Materials

2.1.1. Minefill elements

Tungsten tails attained from a Chinese underground mine were representatively sampled as aggregate. Initially, tailings were dried in a furnace at 100°C for 15 h to ensure test accuracy. Upon completion of the drying process, the tailings were rapidly conserved in a sealed room to prevent the influence of humid air. A laser-based (LS-POP, OMEC, China) particle sizer was adopted to detect its particle size distribution under wet conditions. The tails' chemical composition was analyzed using X-ray fluorescence spectrometer (XRF) (scan speed: 315°·min⁻¹; voltage: 55 kV; current: 135 mA). Fig. 1 demonstrates the physical/chemical findings of the tail specimen.

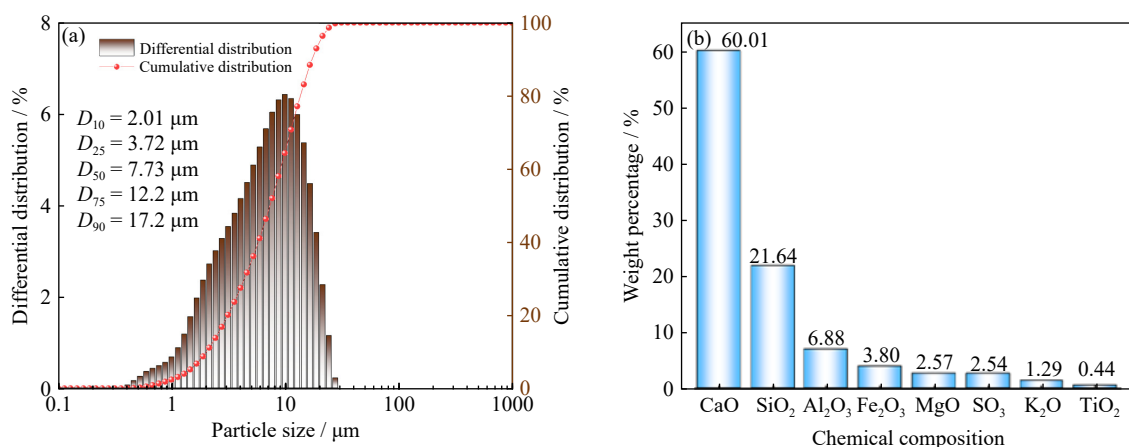


Fig. 1. Particle analysis (a) and chemistry (b) of the cement type adopted.

Ordinary portland cement (OPC) 42.5R produced by a Chinese company was selected as a cementitious material. The laser particle size analyzer and XRF spectrometer were adopted to experimentally test the cement's particle sizes and chemical composition, as demonstrated in Fig. 1. Fig. 1 indicates that the average (D_{50}) and effective (D_{10}) particle sizes

of the cement specimen were 7.73 and 2.01 μm, respectively. Other principal physical properties, such as specific surface area and relative density, were recorded at 1376 m²·kg⁻¹ and 2.7 g·cm⁻³, respectively. The main oxides within the cement were detected as CaO and SiO₂, which accounted for 60.01wt% and 21.64wt%, respectively.

Fig. 2 demonstrates that the D_{50} and D_{10} particle sizes of the tails were 113 and 9.95 μm , respectively. Moreover, the cement's specific surface and relative density values were re-

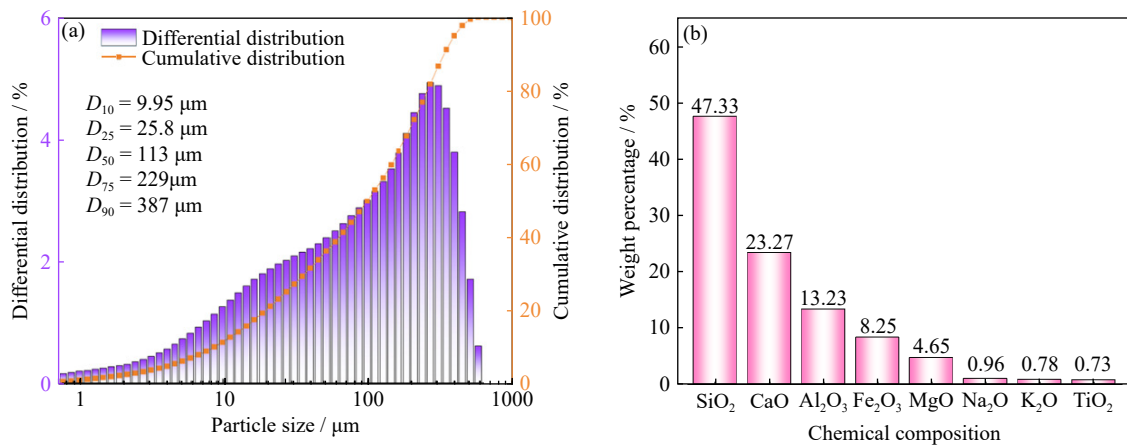


Fig. 2. Grain analysis (a) and chemistry (b) of tails specimen adopted.

The metropolitan water was adopted as mixing water to thoroughly blend the tails and cement. The effect of chemical composition in tap water on the test strength properties was neglected during experiments.

2.1.2. Magnetic induction equipment and steel fiber

In this study, end-hooked steel fibers created by a Chinese (Hebei) firm were used to prepare SFCTBs with a 25 mm fiber length. Table 1 reveals the fiber's specific practical index parameters, whereas Fig. 3 demonstrates its physical morphology.

A steel fiber orientation device suitable for triple square molds is designed in this study, following the preparation method of ring-oriented steel fiber-reinforced cementitious materials in the literature [54]. Fig. 4 shows the magnetic field orientation device. According to Ampere's rule, a uniformly strong magnetic field is shaped in an area enclosed by a helical coil. Moreover, the magnetic induction strength (B) could be adjusted by fine-tuning the current's strength within

corded at $297.6 \text{ m}^2 \cdot \text{kg}^{-1}$ and $3.1 \text{ g} \cdot \text{cm}^{-3}$, respectively. Key oxides in tails were detected as SiO_2 and CaO , accounting for 47.33wt% and 23.27wt%, respectively.

the device, and steel fibers are rotated under an electromagnetic field's action. Magnetic induction strength (B) could be computed using Eq. (1) as follows [39]:

$$B = \frac{\mu_0 n I}{l} \quad (1)$$

where n is the coil's turning number, I indicates the current intensity via wire (A), μ_0 refers to the area's magnetic permeability constant ($4\pi \times 10^{-7}$), and l represents twice the coil's length (m).

The mechanism of the influence of steel fibers and electromagnetic induction strength on the mechanical properties of the filling body lies in the following: steel fibers can bridge the cracks within the filling body, effectively reducing the brittleness of the matrix and improving the toughness of the matrix. In the same way, steel fibers rotate under the action of the applied external electromagnetic field, increasing the orientation coefficient and improving the mechanical properties of the filling body.

Table 1. Summary of technical data of end-hooked steel fiber

Type of steel fiber	Length / mm	Diameter / mm	Length/diameter fraction	Density / ($\text{g} \cdot \text{cm}^{-3}$)	Tensile strength / MPa	Elastic modulus / GPa
End-hooked	25	0.75	33.33	7.75	1.215	195

Fibers incorporated into mortar are affected by gravity, buoyancy, magnetic force and viscous resistance. Moreover, the direction of gravity and buoyancy is vertical, and the ef-



Fig. 3. End-hooked steel fiber's morphology.

fect on fiber orientation is negligible. However, a suitably large magnetic force is required to overcome the effect of viscous resistance and rotate the steel fibers [55]. Fig. 4 demonstrates the distribution of magnetic inductance in the magnetic field orientation device used for trials, as well as in the orientation tool.

2.2. SFCTB sample creating/curing steps

The key goal of the current study is to scrutinize the effect of the direction and rate of steel fiber distribution on the fill's mechanical features. Fill specimens' limits were considered as follows: solid concentration (70wt%), cure age (7 d), cement/tail fraction mass ratio (1:4), whereas steel fiber ratios

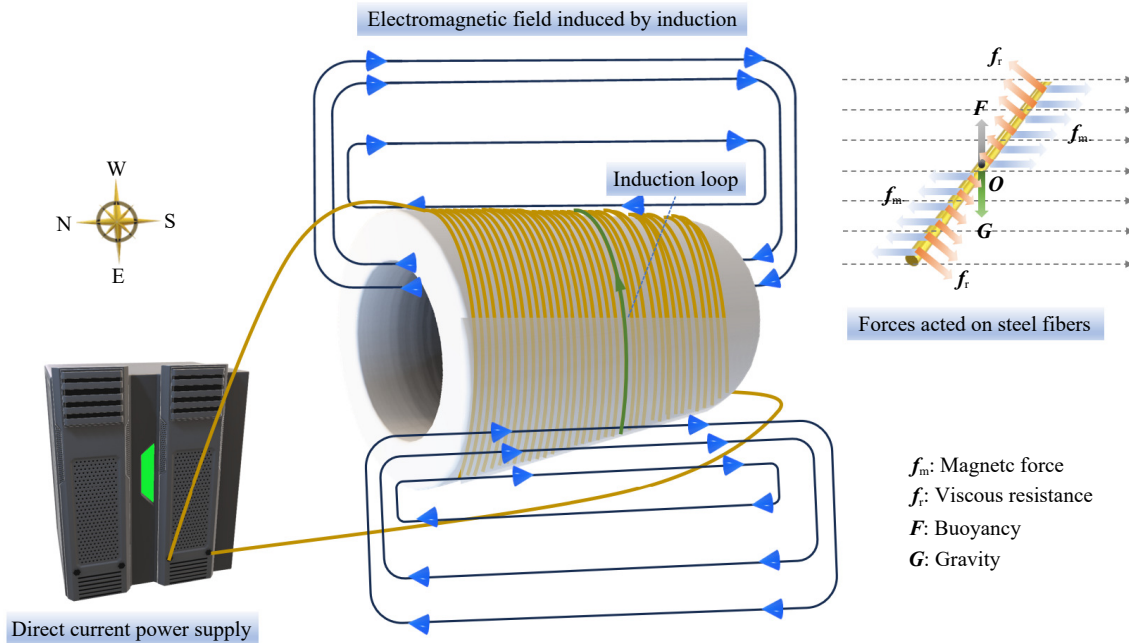


Fig. 4. Magnetic field orientation device used in the test.

were considered as follows: 0 (witness specimen), 0.5vol%, 1.0vol%, 1.5vol%, and 2.0vol%. A total of 51 fill specimens were created by considering three samples for determining the mean results. Table 2 illustrates the fill structure, where group A includes fills without steel fibers added; group B involves fills created at a magnetic induction strength of 0; group C encompasses fills created at a different magnetic induction strength.

Table 2. Lab-made specimens' recipe as a function of magnetic induction and fiber content

Group	Sample number	Magnetic induction strength / (10^{-4} T)	Fiber content / vol%
A	A1	0	0
	B1	0	0.5
	B2	0	1.0
	B3	0	1.5
C	B4	0	2.0
	C1	1	0.5
	C2	2	
	C3	3	
	C4	1	
	C5	2	1.0
	C6	3	
	C7	1	
	C8	2	
	C9	3	1.5
	C10	1	
	C11	2	
C12	3		

For filling specimen preparation, the required materials are initially gathered, the amount of materials for each group is calculated, and the YHC60001 electronic scale is used to

achieve an accurate weight. The raw materials with solid phase are combined into a homogeneous mixture, water is added and mixed well, and then a mortar blender is used for mixing for 3 min. When the slurry achieves the desired fluidity, the steel fibers are gently and evenly joined and then mixed for 3 min until the fibers are evenly circulated. Subsequently, the created fibers are loaded into cubic specimen holders ($70.7 \text{ mm} \times 70.7 \text{ mm} \times 70.7 \text{ mm}$) made of acrylonitrile butadiene styrene (ABS) plastic, and fills are added and allowed to stand for 2–3 min until the fiber is evenly disseminated. Then, the fiber-based fills are placed into these square molds made of ABS plastic upon completion of slurry pouring. In order to steer the steel fibers, the mold is placed in the fiber orientation device and on the vibration table. The orientation device is then activated, with the magnetic induction strength set to $1 (2, 3) \times 10^{-4} \text{ T}$. The slurry is fully vibrated for 2 min. After sufficient vibration, the steel fibers are oriented under the influence of the magnetic field, and then the orientation device is turned off.

Finally, all the fills were cast in a customary-built room for curing, and specimens were de-molded 24 h after casting until the specimens were maintained for 7 d. After complete curing, the fill's upper/lower sides were smoothed and refined, and mechanical tests were conducted, following the measurement of their initial physical limits. Fig. 5 demonstrates the flowchart for creating steel fiber-reinforced fill specimens.

2.3. Strength experiments

Strength trials were undertaken on lab-made specimens with diverse magnetic induction strengths and steel fiber doping to obtain SFCTB's macromechanical limits. The specimens were verified by employing a high-accuracy micro-computer-controlled 5969 universal material test tool (Fig. 6) manufactured by Instron Corporation. The tested SFCTB

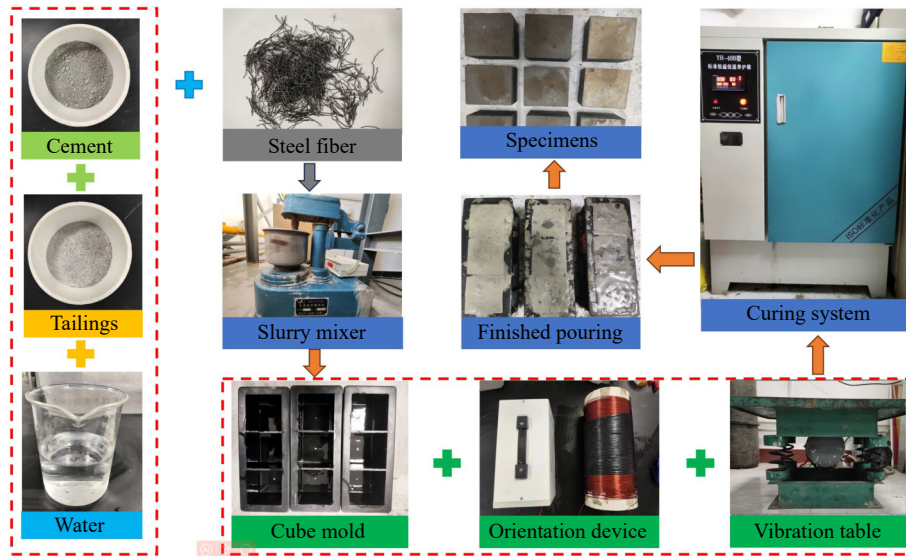


Fig. 5. Critical preparation steps for steel-fiber reinforced cemented tailings backfill specimens.

specimens were sanded and polished prior to the tests to eliminate the effect of surface unevenness on the experiment findings. Throughout the loading process, the load rate was maintained at 1 mm per minute until the specimens were damaged. Meanwhile, all data during the loading process were recorded in real-time and saved in the computer system.

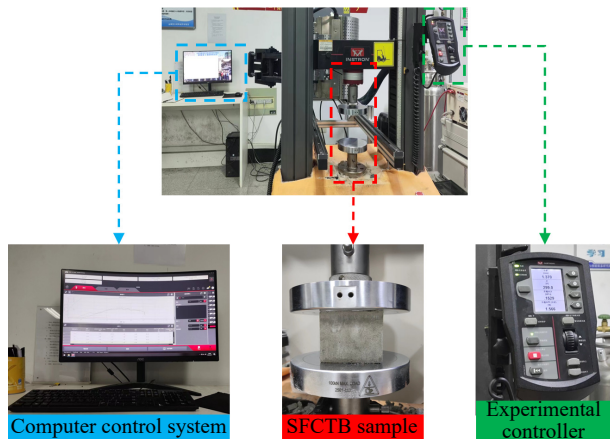


Fig. 6. Working view of the uniaxial compressive test device adopted.

2.4. Dissipated energy’s source

According to thermodynamic codes, material destruction is an energy-driven process of continuous development of internal microcracks, weakening, and eventual loss of strength. When a filling body unit is deformed by an external force, it exhibits no heat alteration by external factors throughout the physical method. Therefore, as indicated by thermodynamics’ first law, energy evolution can be viewed as the change of the entire input energy to elastic strain/strain dissipation energy in fills. Energy in fills subjected to an unconfined compression regime is computed using Eqs. (2)–(4) [56–58], as follows:

$$U = U^e + U^d \tag{2}$$

$$U = \int_0^{\varepsilon_1} \sigma_1 d\varepsilon_1 \tag{3}$$

$$U^e = \frac{1}{2E_u} \sigma_1^2 \tag{4}$$

where U is the total work undertaken by exterior force; U^e refers to the unit releasable elastic strain energy, $\text{MJ}\cdot\text{m}^{-3}$; U^d represents the unit energy dissipation used to create the fill’s inner damage/plastic deformation, $\text{MJ}\cdot\text{m}^{-3}$; E_u denotes the fill’s unloaded elastic modulus, MPa; σ_1 represents the value of stress at a certain moment, MPa; ε_1 represents the value of strain at a certain moment, %. Fig. 7 demonstrates the links between energy dissipation and strain energy [59].

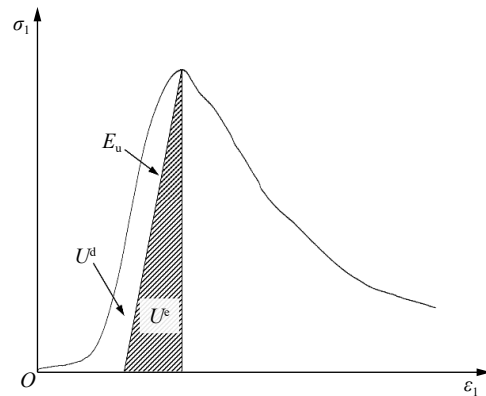


Fig. 7. Energy dissipation vs. strain energy in stress–strain curve.

2.5. SEM microanalysis

At the end of the experimental period, the hydration of the SFCTB samples was terminated using anhydrous ethanol. A Zeiss Gemini 300 SEM tool was employed to test the SFCTB specimens and analyze their internal hydration reactions and microstructural features. The SEM’s operating limits were considered as follows: a maximum quickening volt of up to 30 kV, a maximum amplification of 2000000×, and a maximum resolution of 1 nm. Prior to the experiment, the test samples were dry internally, and then the surfaces were

sprayed with platinum for 4 min using a vacuum coater to improve the electrical conductivity. Fills were positioned in a void hollow for observation after specimen processing was completed.

3. Results and discussion

3.1. Strength features

3.1.1. Steel fiber dosage effect on strength acquisition of SFCTB

Under uniaxial loading test conditions, the peak uniaxial compressive stress (UCS) and peak uniaxial compressive stress increment ratio of SFCTB specimens with the same magnetic induction strength in groups B and C are demonstrated in Fig. 8 compared with the blank control group A. The peak stress of the control group A is 1.99 MPa. Fig. 8 illustrates that the peak stress of SFCTB exhibits an increasing trend by increasing the steel fiber ratio, but with a slight deviation from Fig. 8(c) for steel fiber doping of 1.5vol%. Lab results are optimal when the steel fiber ratio in the matrix is 2.0vol%. Fig. 8(a) shows that for electromagnetic induction strength of 0, the peak stress of SFCTB is smaller than that of control group A when the steel fiber ratio of 0.5vol%–1.5vol%. The primary reason for the effect of the steel fiber ratio on SFCTB may be that when the fiber ratio is small, the steel fiber’s chaotic distribution changes the fill’s original bond strength but does not provide sufficient bridging across

cracks. Fig. 8(b)–(d) indicates that fill’s strengths in all groups are higher than those of control under the premise of maintaining constant magnetic induction strength and increased rates, ranging from 28.43% to 187.94%. The optimum steel fiber ratio is 2.0vol%, and the peak strengths increase by 36.68%, 79.40%, 106.03%, and 187.94% when the magnetic induction strengths are 0, 1×10^{-4} , 2×10^{-4} , and 3×10^{-4} T, respectively, compared with the control group A.

Fill’s strength increase is closely related to fiber incorporation. Fiber has a major role in bridging cracks when the matrix is damaged, reducing the expansion of the cracks and improving the peak stress. Thus, an appropriate quantity of steel fibers can remarkably increase the fill’s peak stress and improve its overall stability, suggesting considerable engineering application value.

3.1.2. Effect of magnetic induction strength on fill’s strength

Fig. 9 shows the link between peak stress and magnetic induction strength of SFCTB specimens compared with the control group A as the steel fiber ratio stabilizes. Similarly, the peak stress of the blank test control group A is 1.99 MPa. Fig. 9 clearly shows that SFCTB peak stress is positively correlated with the magnitude of the magnetic induction strength except at magnetic induction strength of 2×10^{-4} T and steel fiber doping of 2.0vol%.

The steel fibers gradually align and eventually achieve a directional distribution as the magnetic induction strength increases. The peak strength reaches its maximum when the

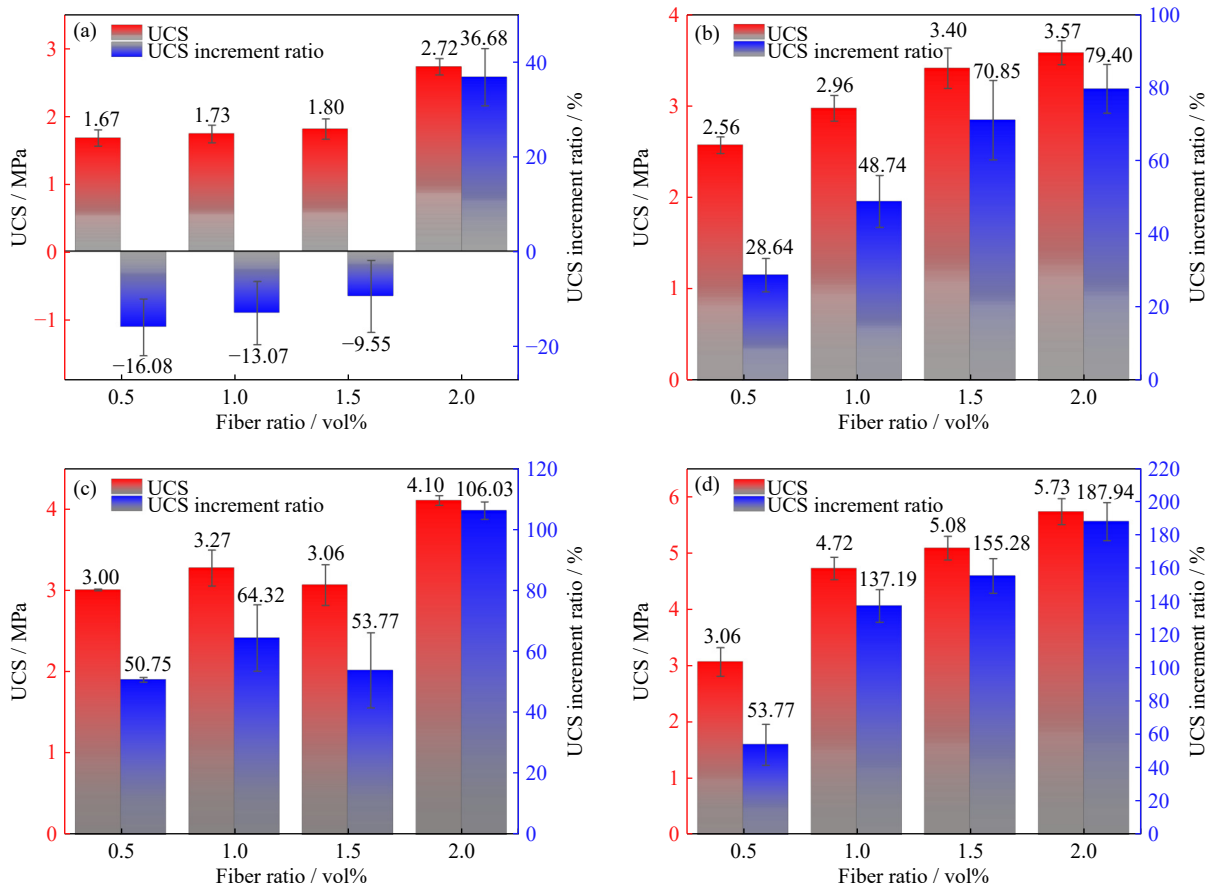


Fig. 8. Average compressive strength of SFCTB at diverse magnetic induction strengths: (a) 0; (b) 1×10^{-4} T; (c) 2×10^{-4} T; (d) 3×10^{-4} T.

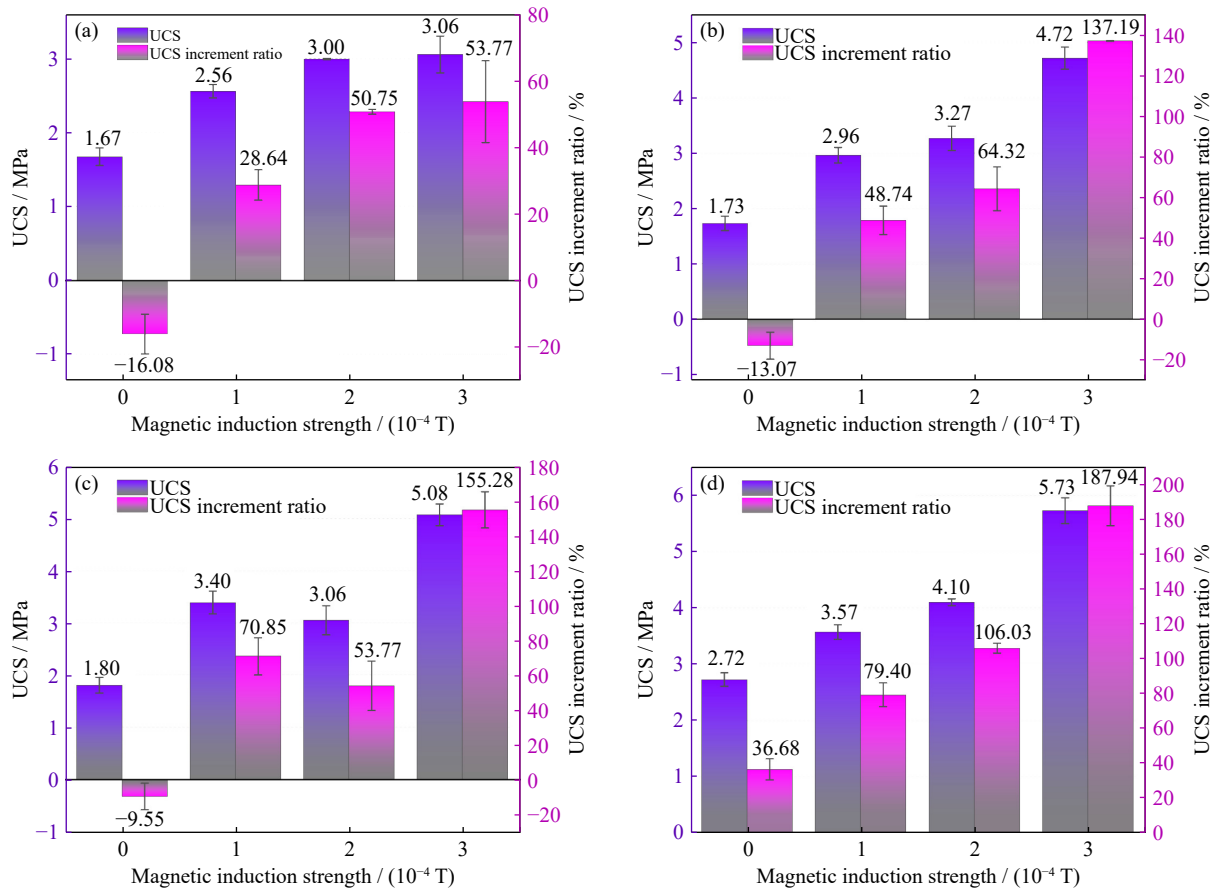


Fig. 9. Average compressive strength of SFCTB with diverse fiber ratios: (a) 0.5vol%; (b) 1.0vol%; (c) 1.5vol%; (d) 2.0vol%.

magnetic induction strength is 3×10^{-4} T, the peak strengths increase by 53.77%, 137.19%, 155.28%, and 187.94% when the steel fiber ratios are 0.5vol%, 1.0vol%, 1.5vol%, and 2.0vol%, respectively, compared with the control group A. Under the same steel fiber doping conditions, increasing magnetic induction strength can improve peak stress except at magnetic induction strength of 2×10^{-4} T and steel fiber doping of 2.0vol%, given that steel fibers within the matrix become aligned. This alignment enhances their interaction with the fill, creating a wrapping effect and allowing the steel fibers to support the load. Simultaneously, during the SFCTB compression phase, bonding between the two forms ensures effective transfer of interface stress and maintains appropriate filling. This effective stress transfer allows the cracked areas of the fill to remain well combined, restraining the development of microcracks within the fill matrix. Consequently, a high deformation capacity is maintained, increasing the fill's peak stress.

3.2. Stress–strain analysis

The curvature of stress–strain variation is among the most imperative pointers of SFCTF's strength features. Fig. 10 demonstrates the link between stress and strain of SFCTB containing diverse fiber ratios for the control group A and constant magnetic induction strength. The damage progression of the specimen can be divided into four stages, as follows: (1) Compression stage: the initial pores inside the specimen gradually close, compacting the fill and reducing its

volume. The curve shows an “upward concave” shape. (2) Linear elasticity stage: the curve appears nearly straight, indicating a linear behavior. At this point, internal changes begin within the SFCTB specimen. (3) Uneven fracture stage: the fill transitions from elastic to plastic deformation. As cracks increase, the UCS gradually reaches its peak. (4) Post-destructive stage: when the SFCTB reaches peak strength, cracks are gradually delayed by increasing load, and the fill specimen is destroyed. However, it retains a certain load-bearing capacity.

Fig. 10 illustrates that when steel fibers are dosed, the amount of stress change in the linear elastic section of the fill's stress and strain curve increases. This change retards the further development of cracks and increases the load-bearing capacity increases as the fill sustains damage. As a result, the steel fiber ratio is generally positively correlated with peak stress.

Moreover, during uniaxial loading, the fill without steel fibers in the control group exhibited brittle damage characteristics, with a rapid decrease in stress following the peak load. On the contrary, with high steel fiber dosage, i.e., 1.0vol%–2.0vol%, SFCTB specimens did not experience a rapid decline in stress after reaching the peak load. This finding indicates that fibers could limit crack growth and enhance SFCTB toughness. This result suggests that adding steel fibers and their steering scattering improve SFCTB's resistance to deformation damage.

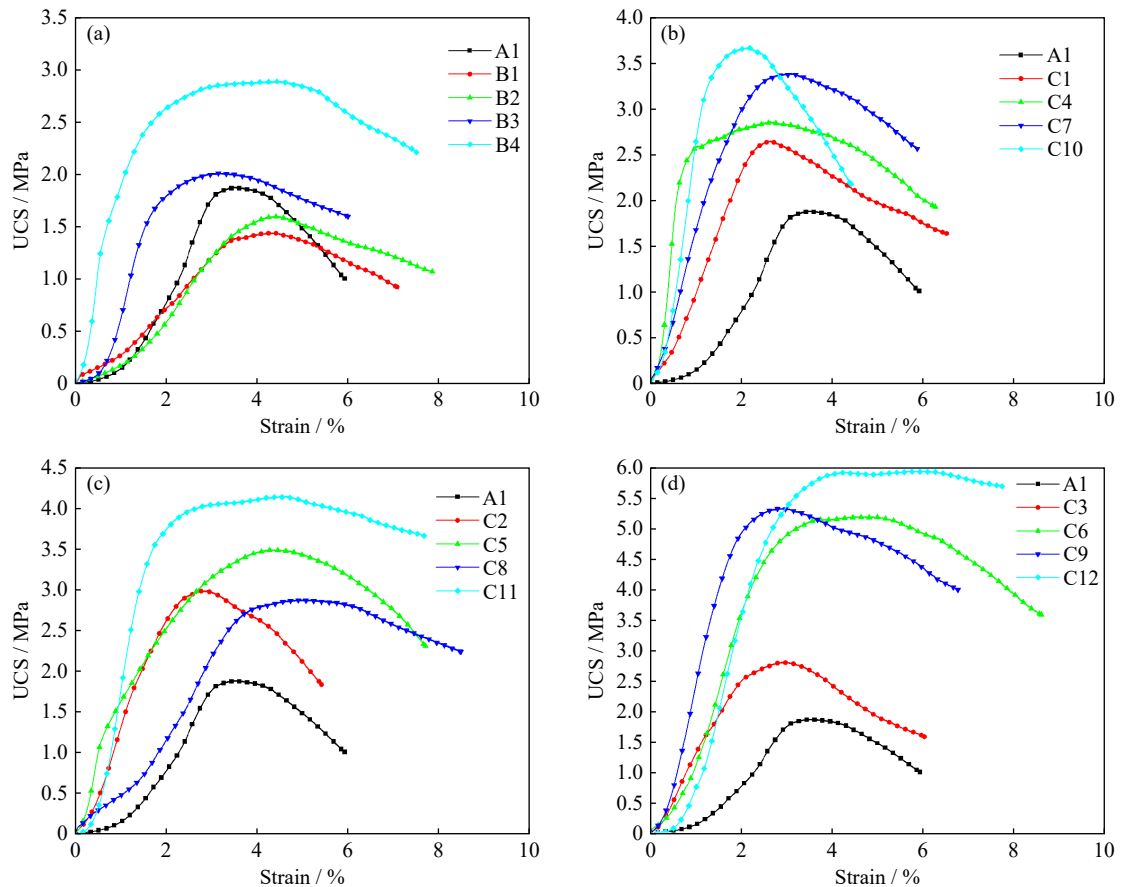


Fig. 10. Stress–strain curve of SFCTB specimens: (a) 0; (b) 1×10^{-4} T; (c) 2×10^{-4} T; and (d) 3×10^{-4} T.

3.3. Fills’ failure styles

Fig. 11 presents the images of the SFCTB specimens during the degradation process at varying fiber doping and magnetic induction strengths. The test results show that the SFCTB specimens exhibited mainly tensile damage, and the crack extension mainly started from the upper section of the filled body and slowly extended downward with the increase in loading until damage occurred. The primary reason for the damage is that the steel fibers are mainly distributed at the bottom of the specimen due to their gravity. Thus, the strength at the bottom is higher and the specimen starts to undergo damage from the top. Fig. 11(e) and (i) demonstrates the degradation process of the clutter-distributed and oriented-distributed SFCTB specimens at a steel fiber doping of 2.0vol%, respectively. During the degradation process, the SFCTB specimens gradually become denser and the strength decreases gradually with time. Moreover, as cracks gradually increase, the sound of steel fibers being pulled out can be heard, and the damage exhibits characteristics of cracking rather than breaking. This condition is mainly because the steel fibers bridge the cracks, enhancing the integrity through their interconnection with the matrix. Furthermore, the bearing capacity of the specimen is effectively improved [60].

3.4. Energy dissipation analysis

The energy evolution features of fills with varying fiber contents and magnetic induction strengths are compared. The

results showed that the change process is similar. Therefore, representative control group A and SFCTBs having diverse steel fiber ratios under magnetic induction strengths of 0 and 3×10^{-4} T, respectively, are selected for analysis. The comparison of stress–strain curve and energy evolution characteristics in Fig. 12 suggests that the energy dissipation can also be analyzed using four stages: (1) Compression stage: the energy captivated by SFCTB from external loads is mostly converted into energy dissipation, which is used for internal pore closure, without elastic strain energy. (2) Linear elasticity stage: a large amount of the energy provided by the external load is converted into elastic strain energy, which is primarily maintained inside the fill. (3) Uneven fracture stage: increasing the external load causes the fill to gradually lose its elasticity and undergo plastic deformation. Moreover, energy dissipation rapidly progresses, and elastic strain energy is diminished. (4) Post-destructive stage: further microcracks appear within the fill, the elastic strain energy is dissipated gradually at a lower level, and the dissipation energy increases substantially.

Fig. 12 also displays that the increase in steel fiber ratios gradually increases the energy U required for fill to reach the destruction. Moreover, at the same steel fiber ratio, greater magnetic induction strength indicates higher energy required for SFCTB specimens to reach the destruction phase. The dissipated strain energy U^d also shows the same trend as the energy U . In general, the energy consumed after rupture increases with increasing in steel fiber ratio and magnetic in-

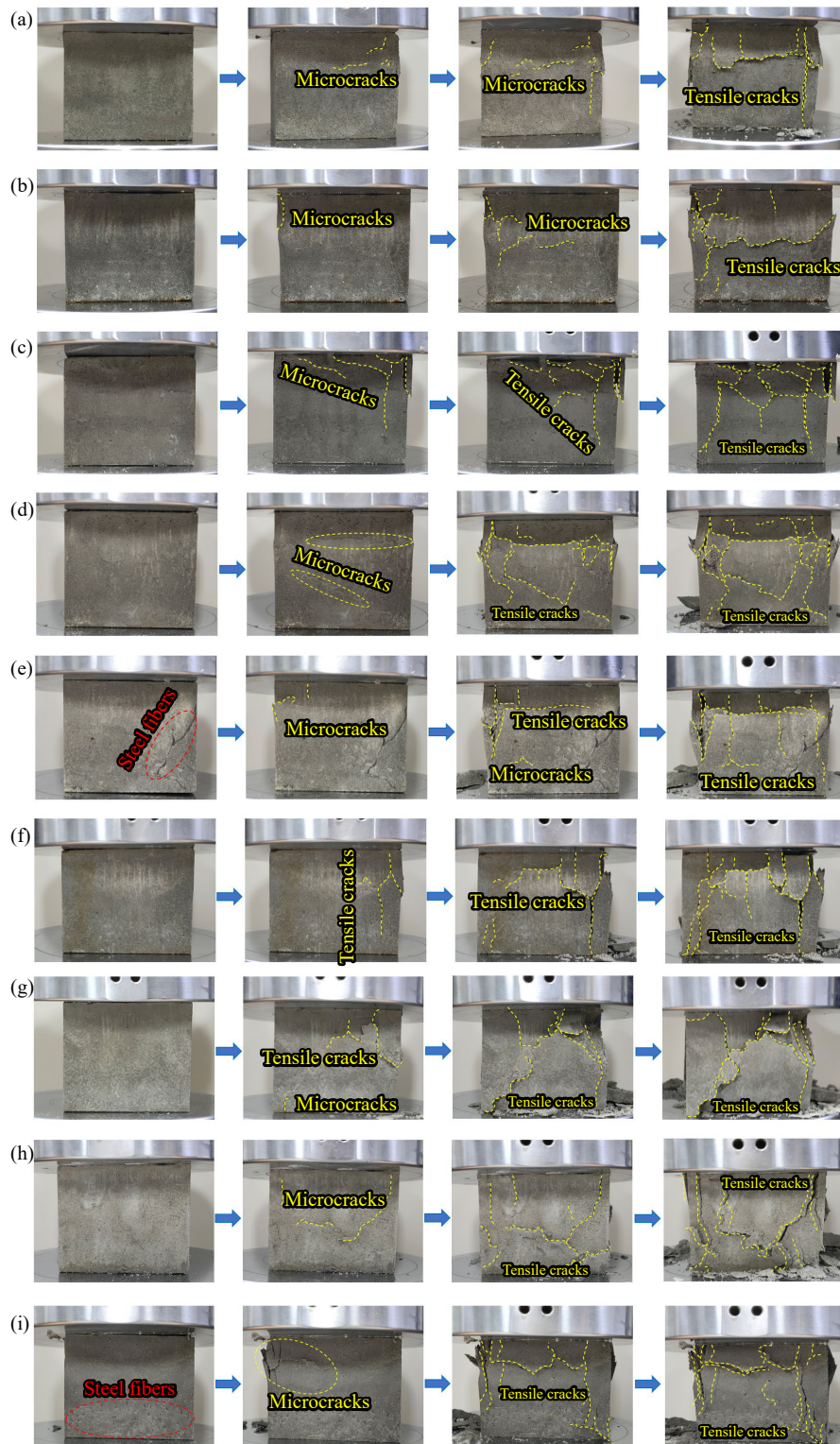


Fig. 11. Damage modes of SFCTB specimens under uniaxial compression conditions: (a) A1; (b) B1; (c) B2; (d) B3; (e) B4; (f) C3; (g) C6; (h) C9; (i) C12.

duction strength. In addition, the elastic strain energy U^e decreases when the specimens reach their peak uniaxial compressive stress. The increase in steel fiber doping and the directional distribution of steel fibers consume more energy mainly because in SFCTB specimens under pressure, the fibers of the filling body enhance the adhesion with the matrix, and the interfacial stresses are transferred to effectively prevent the expansion of cracks within the fills, thereby im-

proving the fills' ability to dissipate energy.

3.5. Microstructure analysis

Small pieces of SFCTB specimens were selected after the uniaxial compressive test to further investigate the internal structure of SFCTB. Subsequently, the SFCTB specimens were immediately seal-soaked using anhydrous ethanol for 24 h to terminate their hydration reaction. Then, seal drying

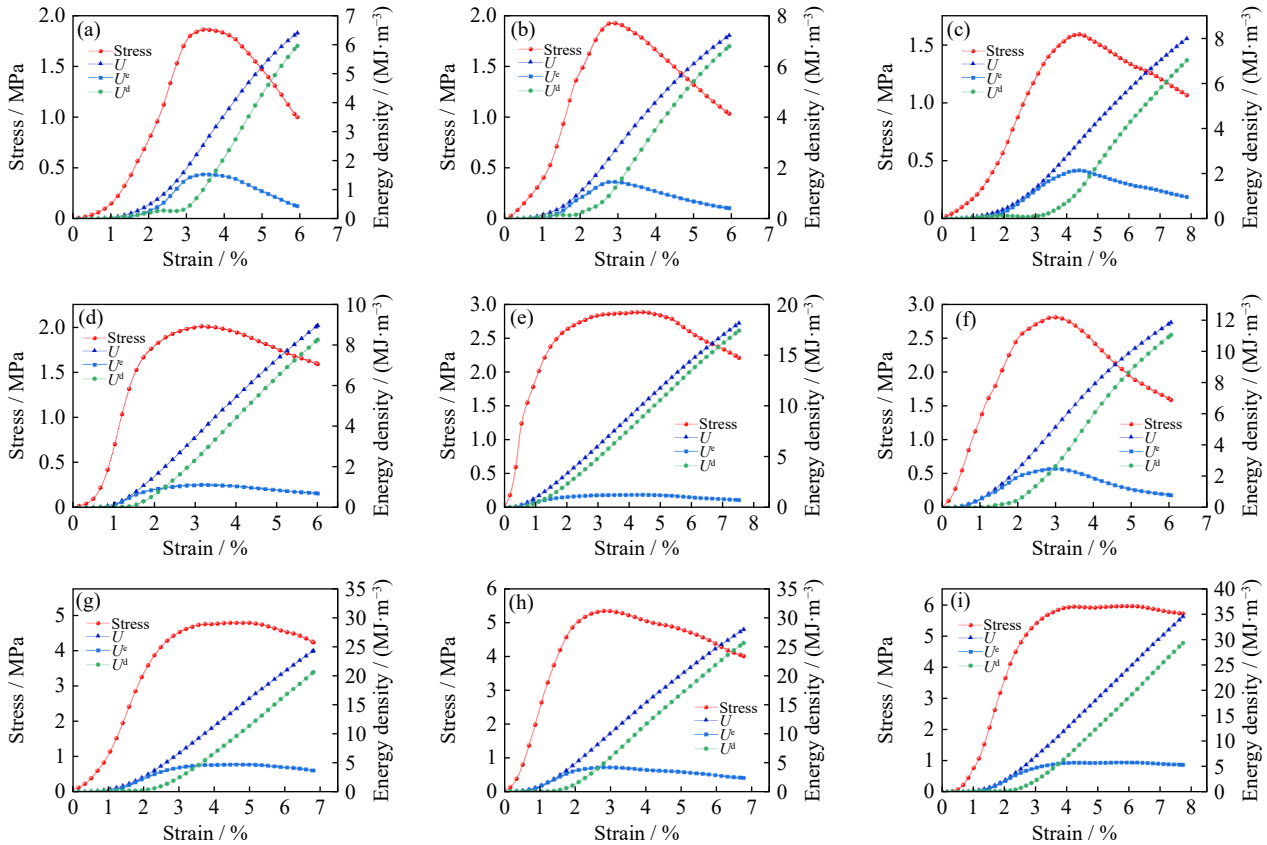


Fig. 12. Energy evolution curves of SFCTB: (a) A1; (b) B1; (c) B2; (d) B3; (e) B4; (f) C3; (g) C6; (h) C9; (i) C12.

was performed at 50°C for 12 h, followed by carbon spraying. Fig. 13 shows the SEM images of fills with diverse steel fiber ratios and magnetic induction strengths. Due to the dimensional properties of the fibers and the fact that they are not prone to fracture, the sections containing steel fibers were purposely avoided in the specimens observed. Fig. 13 also demonstrates that the hydration conditions of each substance within the fill produced a large number of hydrating products, including needle-like Aft ($3\text{CaO}\cdot\text{Al}_2\text{O}_3\cdot 3\text{CaSO}_4\cdot 32\text{H}_2\text{O}$), fibrous C-S-H ($x\text{CaO}\cdot\text{SiO}_2\cdot y\text{H}_2\text{O}$) gel, and $\text{Ca}(\text{OH})_2$ in lamellar and flake structures. These products interlocked with each other, ultimately increasing the strength of SFCTB. Many pores and unhydrated tailings crystal particles were observed, and the specimens doped with steel fibers produced more pores. Fig. 13(a), (e)–(g), and (i) clearly shows that the cross-climbing of the fibrous C-S-H gel formed during hydration connects originally dispersed cement particles, tailings particles, and their hydration products. This interaction creates a three dimensional (3D) and structurally dense matrix that reduces pore spaces, thereby enhancing the SFCTB’s strength after curing. Fig. 13(b)–(d), and (h) illustrates that the $\text{Ca}(\text{OH})_2$ is formed during hydration reaction, with extremely low strength and poor stability. $\text{Ca}(\text{OH})_2$ is the first component to be eroded, mostly enriched at the boundary of cement particles and tail grains, and crystallizes into coarse grains. Consequently, the reduced adhesion at the interface becomes the weakest link in the fill’s degradation process [61].

Figs. 14 and 15 show the major element mapping distributions, EDS (energy dispersive spectrometer) spectra maps,

and major element percentages for specimens A1 and C9, respectively. The figures illustrate that the major elements of the SFCTB specimens are O, Ca, C, Si, and Al for specimen A1 and O, C, Ca, Si, and Mg for specimen C9. Moreover, O, C, Ca, and Si are the four most dominant elements, which are heavily clustered around CSH gel, resulting in a remarkably higher strength of the SFCTB specimens.

4. Conclusions

UCS experiments and SEM observations were carried out on varying types of SFCTBs to explore the effects of steel fiber ratio and magnetic induction strength on SFCTB’s microstructure and strength features, determining the fills’ mechanical/microstructural evolution. On the basis of experimental outcomes, the subsequent assumptions were obtained.

(1) SFCTB’s main damage mode is tensile, and the crack expansion mainly starts from the fill’s upper section and gradually expands downward with the increase in load until the damage occurs.

(2) When the steel fiber ratio is 2.0vol%, SFCTB solidifies during destruction, such as cracking, but not breaking.

(3) As fiber ratio and magnetic induction strength increase, relatively high energy is required for SFCTB to reach its destruction.

(4) Fiber insertion enhances the bond between the fill and the interface, effectively preventing the expansion of cracks in the fill and improving the energy dissipation capacity of the fill.

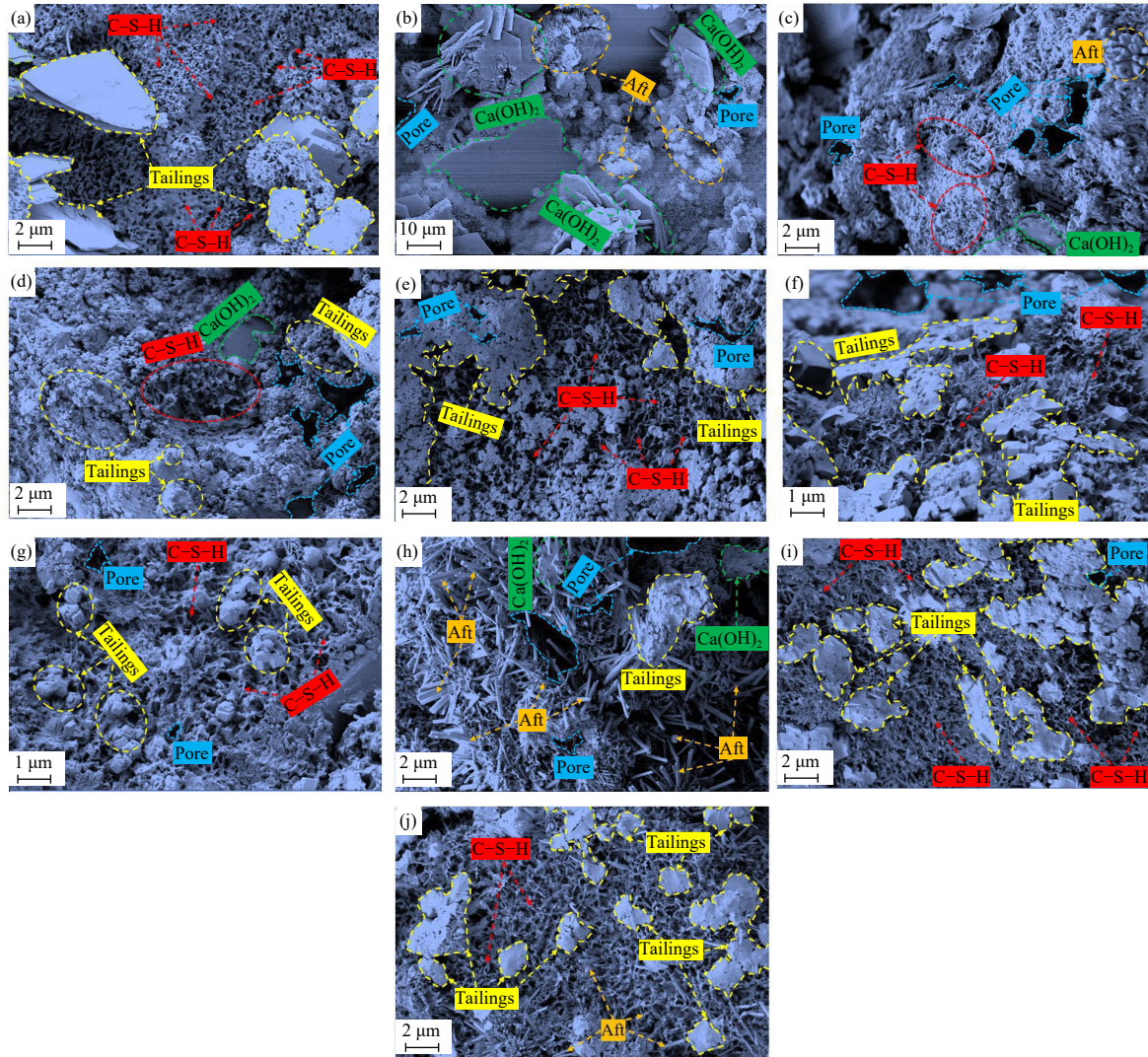


Fig. 13. SFCTB's SEM images: (a) and (b) are different positions of A1; (c) B1; (d) B2; (e) B3; (f) B4; (g) C3; (h) C6; (i) C9; (j) C12.

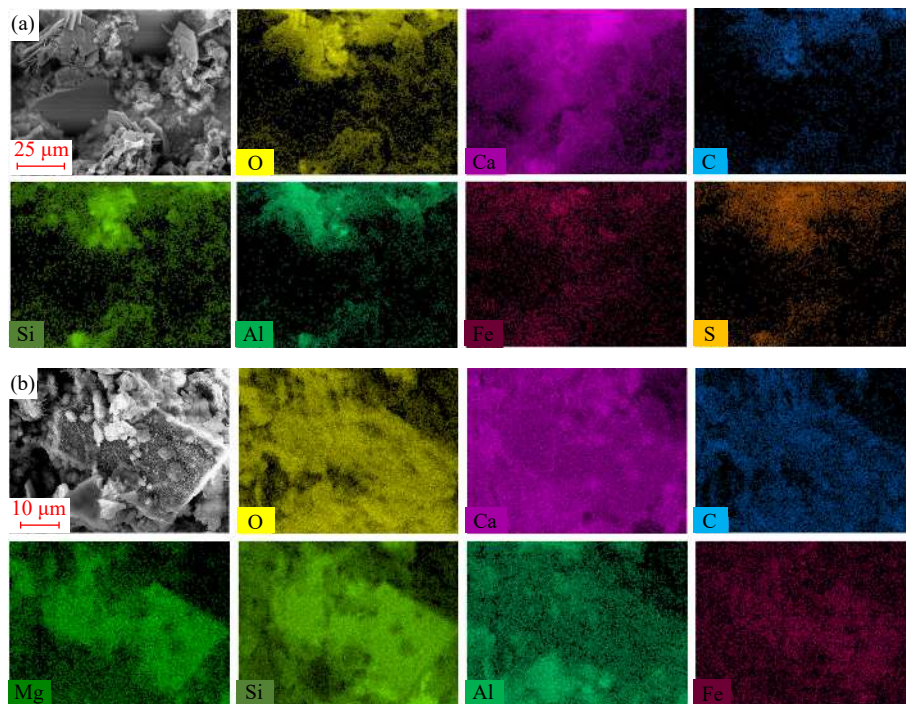


Fig. 14. Major element mapping distribution of SFCTB specimens: (a) A1; (b) C9.

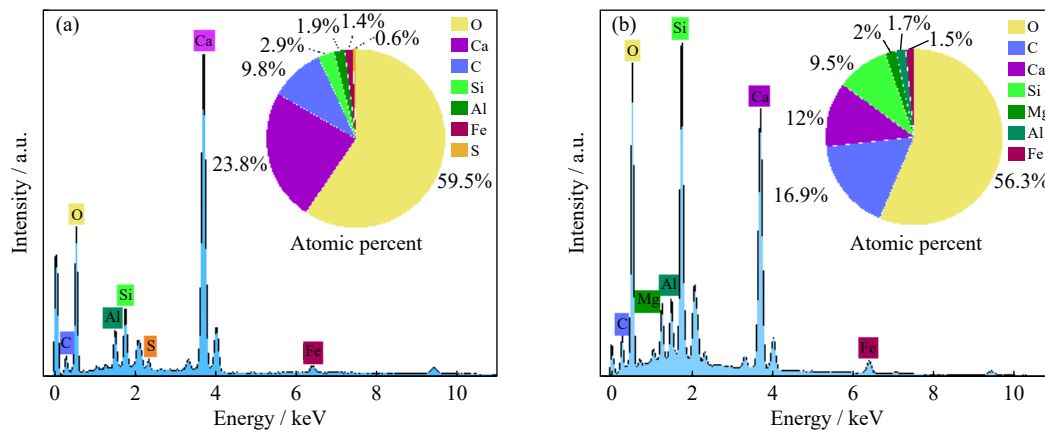


Fig. 15. EDS spectra and major element percentages of SFCTB: (a) A1; (b) C9.

Acknowledgements

This work was financially supported by the China's National Key Research and Development Program (No. 2022YFC2905004) and the China Postdoctoral Science Foundation (No. 2023M742134).

Conflict of Interest

Shuai Cao is an editorial board member for this journal and was not involved in the editorial review or the decision to publish this article. All authors do not have competing interests to declare.

References

- [1] L.H. Yang, J.C. Li, H.B. Liu, *et al.*, Systematic review of mixing technology for recycling waste tailings as cemented paste backfill in mines in China, *Int. J. Miner. Metall. Mater.*, 30(2023), No. 8, p. 1430.
- [2] A. Fernández, P. Segarra, J.A. Sanchidrián, and R. Navarro, Ore/waste identification in underground mining through geochemical calibration of drilling data using machine learning techniques, *Ore Geol. Rev.*, 168(2024), art. No. 106045.
- [3] D.W. Li, A.O. Ramos, A. Bah, and F.H. Li, Valorization of lead-zinc mine tailing waste through geopolymerization: Synthesis, mechanical, and microstructural properties, *J. Environ. Manage.*, 349(2024), art. No. 119501.
- [4] Y. Xu, Y.J. Han, G.Q. Zhao, and S.Y. Meng, Enhancing geotechnical reinforcement: Exploring molybdenum tailings and basalt fibre-modified composites for sustainable construction, *Constr. Build. Mater.*, 411(2024), art. No. 134452.
- [5] H. Qin, S. Cao, and E. Yilmaz, Mechanical, energy evolution, damage and microstructural behavior of cemented tailings-rock fill considering rock content and size effects, *Constr. Build. Mater.*, 411(2024), art. No. 134449.
- [6] Y.K. Liu, Y.M. Wang, and Q.S. Chen, Using cemented paste backfill to tackle the phosphogypsum stockpile in China: A down-to-earth technology with new vitalities in pollutant retention and CO₂ abatement, *Int. J. Miner. Metall. Mater.*, 31(2024), No. 7, p. 1480.
- [7] S. Cao, G.L. Xue, E. Yilmaz, and Z.Y. Yin, Assessment of rheological and sedimentation characteristics of fresh cemented tailings backfill slurry, *Int. J. Min. Reclam. Environ.*, 35(2021), No. 5, p. 319.
- [8] G.L. Xue, E. Yilmaz, and Y.D. Wang, Progress and prospects of mining with backfill in metal mines in China, *Int. J. Miner. Metall. Mater.*, 30(2023), No. 8, p. 1455.
- [9] A.X. Wu, Z.Q. Wang, Z.E. Ruan, R. Bürger, S.Y. Wang, and Y. Mo, Rheological properties and concentration evolution of thickened tailings under the coupling effect of compression and shear, *Int. J. Miner. Metall. Mater.*, 31(2024), No. 5, p. 862.
- [10] R.G. Gao, W.J. Wang, X. Xiong, J.J. Li, and C. Xu, Effect of curing temperature on the mechanical properties and pore structure of cemented backfill materials with waste rock-tailings, *Constr. Build. Mater.*, 409(2023), art. No. 133850.
- [11] J. Wang, Q.J. Yu, Z.Z. Xiang, J.X. Fu, L.M. Wang, and W.D. Song, Influence of basalt fiber on pore structure, mechanical performance and damage evolution of cemented tailings backfill, *J. Mater. Res. Technol.*, 27(2023), p. 5227.
- [12] J.J. Li, S. Cao, and E. Yilmaz, Characterization of macro mechanical properties and microstructures of cement-based composites prepared from fly ash, gypsum and steel slag, *Minerals*, 12(2021), No. 1, art. No. 6.
- [13] Q.L. Li, B.W. Wang, L. Yang, *et al.*, Synthesis of cemented paste backfill by reutilizing multiple industrial waste residues and ultrafine tailings: Strength, microstructure, and GA-GPR prediction modeling, *Powder Technol.*, 434(2024), art. No. 119337.
- [14] S.C. Wu, T.C. Sun, J. Kou, H. Li, and E.X. Gao, Green and efficient recovery of poly metals from converter sludge through reduction roasting and preparation of backfill from tailings, *Chem. Eng. J.*, 479(2024), art. No. 147582.
- [15] K.Z. Xia, C.X. Chen, X.M. Liu, Y. Wang, X.T. Liu, and J.H. Yuan, Estimating shear strength of high-level pillars supported with cemented backfilling using the Hoek–Brown strength criterion, *J. Rock Mech. Geotech. Eng.*, 16(2024), No. 2, p. 454.
- [16] T. Kasap, E. Yilmaz, and M. Sari, Physico-chemical and microstructural behavior of cemented mine backfill: Effect of pH in dam tailings, *J. Environ. Manage.*, 314(2022), art. No. 115034.
- [17] W.J. Liu, Z.X. Liu, S. Xiong, and M. Wang, Comparative prediction performance of the strength of a new type of Ti tailings cemented backfilling body using PSO-RF, SSA-RF, and WOA-RF models, *Case Stud. Constr. Mater.*, 20(2024), art. No. e02766.
- [18] Z.Q. Huang, S. Cao, and E. Yilmaz, Microstructure and mechanical behavior of cemented gold/tungsten mine tailings-crushed rock backfill: Effects of rock gradation and content, *J. Environ. Manage.*, 339(2023), art. No. 117897.
- [19] J.J. Li, S. Cao, and E. Yilmaz, Reinforcing effects of polypropylene on energy absorption and fracturing of cement-based tailings backfill under impact loading, *Int. J. Miner. Metall. Mater.*, 31(2024), No. 4, p. 650.
- [20] H.B. Liu and M. Fall, Testing the properties of cemented tailings backfill under multiaxial compressive loading, *Constr. Build. Mater.*, 421(2024), art. No. 135682.

- [21] X. Zhang, X.L. Xue, D.X. Ding, P.C. Sun, J.L. Li, and Y. He, A study of the mechanical properties, environmental effect, and microscopic mechanism of phosphorus slag-based uranium tailings backfilling materials, *J. Cleaner Prod.*, 446(2024), art. No. 141306.
- [22] S.X. Zou, S. Cao, and E. Yilmaz, Enhancing flexural property and mesoscopic mechanism of cementitious tailings backfill fabricated with 3D-printed polymers, *Constr. Build. Mater.*, 414(2024), art. No. 135009.
- [23] X.P. Song, Y.C. Huang, S. Wang, H.G. Yu, and Y.X. Hao, Macro-mesoscopic mechanical properties and damage progression of cemented tailings backfill under cyclic static load disturbance, *Compos. Struct.*, 322(2023), art. No. 117433.
- [24] Y.Y. Wang, Z.Q. Yu, and H.W. Wang, Experimental investigation on some performance of rubber fiber modified cemented paste backfill, *Constr. Build. Mater.*, 271(2021), art. No. 121586.
- [25] A.A. Wang, S. Cao, and E. Yilmaz, Quantitative analysis of pore characteristics of nanocellulose reinforced cementitious tailings fills using 3D reconstruction of CT images, *J. Mater. Res. Technol.*, 26(2023), p. 1428.
- [26] B. Zhang, K.Q. Li, R.J. Cai, H.B. Liu, Y.F. Hu, and B. Han, Properties of modified superfine tailings cemented paste backfill: Effects of mixing time and Al₂O₃ dosage, *Constr. Build. Mater.*, 417(2024), art. No. 135365.
- [27] J.J. Li, S. Cao, and W.D. Song, Flexural behavior of cementitious backfill composites reinforced by various 3D printed polymeric lattices, *Compos. Struct.*, 323(2023), art. No. 117489.
- [28] M. Chen, H. Zhong, H. Wang, and M.Z. Zhang, Behaviour of recycled tyre polymer fibre reinforced concrete under dynamic splitting tension, *Cem. Concr. Compos.*, 114(2020), art. No. 103764.
- [29] S.Z. Zou, W.H. Guo, S. Wang, Y.T. Gao, L.Y. Qian, and Y. Zhou, Investigation of the dynamic mechanical properties and damage mechanisms of fiber-reinforced cemented tailing backfill under triaxial split-Hopkinson pressure bar testing, *J. Mater. Res. Technol.*, 27(2023), p. 105.
- [30] X.H. Li, S. Cao, and E. Yilmaz, Effect of magnetic induction intensity and steel fiber rate on strength improvement of cementitious filling composites, *Constr. Build. Mater.*, 428(2024), art. No. 136417.
- [31] K. Zhao, Y.M. Lai, Z.W. He, *et al.*, Study on energy dissipation and acoustic emission characteristics of fiber tailings cemented backfill with different ash-sand ratios, *Process Saf. Environ. Prot.*, 174(2023), p. 983.
- [32] L. Cui and A. McAdie, Experimental study on evolutive fracture behavior and properties of sulfate-rich fiber-reinforced cemented paste backfill under pure mode-I, mode-II, and mode-III loadings, *Int. J. Rock Mech. Min. Sci.*, 169(2023), art. No. 105434.
- [33] G.L. Xue, E. Yilmaz, G.R. Feng, and S. Cao, Bending behavior and failure mode of cemented tailings backfill composites incorporating different fibers for sustainable construction, *Constr. Build. Mater.*, 289(2021), art. No. 123163.
- [34] G.L. Xue, E. Yilmaz, W.D. Song, and S. Cao, Mechanical, flexural and microstructural properties of cement-tailings matrix composites: Effects of fiber type and dosage, *Composites Part B*, 172(2019), p. 131.
- [35] Z.Q. Huang, S. Cao, and E. Yilmaz, Investigation on the flexural strength, failure pattern and microstructural characteristics of combined fibers reinforced cemented tailings backfill, *Constr. Build. Mater.*, 300(2021), art. No. 124005.
- [36] S. Wang, X.P. Song, M.L. Wei, *et al.*, Strength characteristics and microstructure evolution of cemented tailings backfill with rice straw ash as an alternative binder, *Constr. Build. Mater.*, 297(2021), art. No. 123780.
- [37] Z.B. Guo, J.P. Qiu, A. Kirichek, H. Zhou, C. Liu, and L. Yang, Recycling waste tyre polymer for production of fibre reinforced cemented tailings backfill in green mining, *Sci. Total Environ.*, 908(2024), art. No. 168320.
- [38] S-T. Kang and J-K. Kim, The relation between fiber orientation and tensile behavior in an ultra high performance fiber reinforced cementitious composites (UHPRCC), *Cem. Concr. Res.*, 41 (2011), No. 10, p.1001.
- [39] M.M. Al Rifai, K.S. Sikora, and M.N.S. Hadi, Magnetic alignment of micro steel fibers embedded in self-compacting concrete, *Constr. Build. Mater.*, 412(2024), art. No. 134796.
- [40] H. Zhang, S. Cao, and E. Yilmaz, Influence of 3D-printed polymer structures on dynamic splitting and crack propagation behavior of cementitious tailings backfill, *Constr. Build. Mater.*, 343(2022), art. No. 128137.
- [41] Y.A. Li, W.H. Zhang, G.W. Sun, *et al.*, A new orientational molding method for ultra-high performance concrete with high content of steel fiber and investigation on its flexure and axial tensile properties, *Constr. Build. Mater.*, 400(2023), art. No. 132755.
- [42] M.J.H. Wijffels, R.J.M. Wolfs, A.S.J. Suiker, and T.A.M. Salet, Magnetic orientation of steel fibres in self-compacting concrete beams: Effect on failure behaviour, *Cem. Concr. Compos.*, 80(2017), p. 342.
- [43] X.H. Zhang, F.B. He, J. Chen, C.Q. Yang, and F. Xu, Orientation of steel fibers in concrete attracted by magnetized rebar and its effects on bond behavior, *Cem. Concr. Compos.*, 138(2023), art. No. 104977.
- [44] Y.X. Zheng, X.M. Lv, S.W. Hu, J.B. Zhuo, C. Wan, and J.Q. Liu, Mechanical properties and durability of steel fiber reinforced concrete: A review, *J. Build. Eng.*, 82(2024), art. No. 108025.
- [45] S.Q. Meng, C.J. Jiao, X.W. Ouyang, Y.F. Niu, and J.Y. Fu, Effect of steel fiber-volume fraction and distribution on flexural behavior of Ultra-high performance fiber reinforced concrete by digital image correlation technique, *Constr. Build. Mater.*, 320(2022), art. No. 126281.
- [46] H. Zhang, Y.J. Huang, M. Lin, and Z.J. Yang, Effects of fibre orientation on tensile properties of ultra high performance fibre reinforced concrete based on meso-scale Monte Carlo simulations, *Compos. Struct.*, 287(2022), art. No. 115331.
- [47] H.H. Huang, X.J. Gao, L.S. Li, and H. Wang, Improvement effect of steel fiber orientation control on mechanical performance of UHPC, *Constr. Build. Mater.*, 188(2018), p. 709.
- [48] F. Javahershenas, M.S. Gilani, and M. Hajforoush, Effect of magnetic field exposure time on mechanical and microstructure properties of steel fiber-reinforced concrete (SFRC), *J. Build. Eng.*, 35(2021), art. No. 101975.
- [49] D.Y. Yoo, S.T. Kang, N. Banthia, and Y.S. Yoon, Nonlinear finite element analysis of ultra-high-performance fiber-reinforced concrete beams, *Int. J. Damage Mech.*, 26(2017), No. 5, p. 735.
- [50] L.B. Qing, H.L. Sun, Y.B. Zhang, R. Mu, and M.D. Bi, Research progress on aligned fiber reinforced cement-based composites, *Constr. Build. Mater.*, 363(2023), art. No. 129578.
- [51] H. Li, L. Li, J. Zhou, R. Mu, and M.F. Xu, Influence of fiber orientation on the microstructures of interfacial transition zones and pull-out behavior of steel fiber in cementitious composites, *Cem. Concr. Compos.*, 128(2022), art. No. 104459.
- [52] R. Mu, J. Chen, X.S. Chen, C.R. Diao, X.W. Wang, and L.B. Qing, Effect of the orientation of steel fiber on the strength of ultra-high-performance concrete (UHPC), *Constr. Build. Mater.*, 406(2023), art. No. 133431.
- [53] R. Mu, C.R. Diao, H.Q. Liu, *et al.*, Design, preparation and mechanical properties of full-field aligned steel fiber reinforced cementitious composite, *Constr. Build. Mater.*, 272(2021), art. No. 121631.
- [54] L. Ke, L.M. Liang, Z. Feng, C.X. Li, J.L. Zhou, and Y.L. Li,

- Bond performance of CFRP bars embedded in UHPFRC incorporating orientation and content of steel fibers, *J. Build. Eng.*, 73(2023), art. No. 106827.
- [55] G.D. Cao, Z.J. Li, S.Q. Jiang, et al., Experimental analysis and numerical simulation of flow behavior of fresh steel fibre reinforced concrete in magnetic field, *Constr. Build. Mater.*, 347(2022), art. No. 128505.
- [56] Y.Q. Hou, S.H. Yin, X. Chen, M.Z. Zhang, and S.X. Yang, Study on characteristic stress and energy damage evolution mechanism of cemented tailings backfill under uniaxial compression, *Constr. Build. Mater.*, 301(2021), art. No. 124333.
- [57] X.P. Song, J.B. Li, S. Wang, et al., Study of mechanical behavior and cracking mechanism of prefabricated fracture cemented paste backfill under different loading rates from the perspective of energy evolution, *Constr. Build. Mater.*, 361(2022), art. No. 129737.
- [58] C.L. Wang, G.Y. Du, E.B. Li, X. Sun, and Y. Pan, Evolution of strength parameters and energy dissipation of Beishan deep granite under conventional triaxial compression, *Chin J Rock Mech. Eng.*, 40(2021), No. 11, p. 2238.
- [59] K. Zhao, X. Yu, Y. Zhou, Q. Wang, J.Q. Wang, and J.L. Hao, Energy evolution of brittle granite under different loading rates, *Int. J. Rock Mech. Min. Sci.*, 132(2020), art. No. 104392.
- [60] B.X. Yan, H.W. Jia, E. Yilmaz, X.P. Lai, P.F. Shan, and C. Hou, Numerical study on microscale and macroscale strength behaviors of hardening cemented paste backfill, *Constr. Build. Mater.*, 321(2022), art. No. 126327.
- [61] P. Yan, B. Chen, M.Z. Zhu, and X.R. Meng, Study on mechanical properties and microstructure of green ultra-high performance concrete prepared by recycling waste glass powder, *J. Build. Eng.*, 82(2024), art. No. 108206.